PERGAMON

Computers & Geosciences 25 (1999) 695–704

COMPUTERS & GEOSCIENCES

RNGCHN: a program to calculate displacement components from dislocations in an elastic half-space with applications for modeling geodetic measurements of crustal deformation ☆

Kurt L. Feigl*, Emmeline Dupré

UMR 5562, Centre National de la Recherche Scientifique, 14, Avenue Edouard Belin, 31400, Toulouse, France

Received 22 July 1996; received in revised form 18 November 1998; accepted 18 November 1998

Abstract

The RNGCHN program calculates a single component of the displacement field due to a finite or point-source dislocation buried in an elastic half space. This formulation approximates the surface movements produced by earthquake faulting or volcanic intrusion. As such, it is appropriate for modeling crustal deformation measured by geodetic surveying techniques, such as spirit leveling, trilateration, Very Long Baseline Interferometry (VLBI), Global Positioning System (GPS), or especially interferometric analysis of synthetic aperture radar (SAR) images. Examples suggest that this model can fit simple coseismic earthquake signatures to within their measurement uncertainties. The program's input parameters include fault position, depth, length, width, strike, dip, and three components of slip. The output consists of displacement components in the form of an ASCII list or a rectangular array of binary integers. The same program also provides partial derivatives of the displacement component with respect to all 10 input parameters. The FORTRAN source code for the program is in the public domain and available as the compressed tar file rngchn.tar.Z in the directory/pub/GRGS via the Internet by anonymous ftp to spike.cst. cnes.fr. This distribution includes worked examples and a MATLAB interface.

Keywords: Faults; Geodesy; Fortran

1. Introduction

With the advent of precise surveying techniques, geophysicists now routinely measure the Earth as it deforms beneath their feet. Earthquake movements of the ground surface, usually called 'coseismic displacements', seem to interest the public because they are sudden, permanent and dangerous. To the geophysicist, they provide information about the seismic source on the fault. Yet measurements of coseismic displacements are rare because they require an observation before the earthquake occurs. Moreover, a survey station must be near the epicenter to experience significant permanent displacement, because the magnitude of the signal decays with the inverse square of the dis-

☆ Code available at http://www.iamg.org/CGEditor/index.htm

* Corresponding author. Tel.: +33 561 33 29 40; fax: +33 561 25 32 05.

E-mail address: kurt.feigl@cnes.fr (K.L. Feigl)

0098-3004/99/$ - see front matter
PII: S0098-3004(99)00003-5

Table 1
Notation

Quantity	Symbol	Units
Range change	$\Delta\rho$	mm
Slip vector on fault (left-lateral, up-dip, tensile)	$\mathbf{U}$	mm
Dip of fault (from horizontal)	δ	degrees
Strike of fault (azimuth taken clockwise from North)	α	degrees
Width of fault patch along dip	W	km
Length of fault patch along strike	L	km
Coordinates of lower-left corner of fault patch (East, North, depth)	$[X, Y, d]$	km
Displacement vector at surface (East, North, up)	$\mathbf{u}$	mm
Coordinates of point on ground surface (East, North)	$[E, N]$	km
Unit 'look' vector pointing from ground to satellite (East, North, up)	$\hat{\mathbf{s}}$	–
Elastic (Lamé) coefficients	λ, μ	Pa s
Rake of slip vector (from horizontal in fault plane)	r	degrees
Coordinates of centroid of fault patch (East, North, depth)	$[X_C, Y_C, d_C]$	km
Locking depth	D	km
Seismic moment	M_0	N m
Large numerical value	B	km

tance from the earthquake source (Aki and Richards, 1980). Nonetheless, repeated surveys of geodetic networks have successfully measured coseismic displacements in several dozen cases by spirit leveling (Lin and Stein, 1989), trilateration (Savage, 1983), Very Long Baseline Interferometry (VLBI) (Clark et al., 1990), or the Global Positioning System (GPS) (Hudnut et al., 1994), for which we cite only a few studies of earthquakes in California as examples.

More recently, satellite radar interferometry has removed the requirement for measurement stations on the ground, greatly increasing the number of measurement points. In a spectacular demonstration, the ERS-1 satellite captured the entire coseismic deformation field of the 1992 Landers earthquake (Massonnet et al., 1993, 1994; Zebker et al., 1994). This new geodetic technique compares the phase in synthetic aperture radar (SAR) images acquired before and after a crustal deformation event to measure the change in range (line of sight distance) from satellite to ground (Massonnet and Feigl, 1998) http://www-project.cst.cnes.fr:8060/radar/Mission.html http://www.asf.alaska.edu http://www.itc.nl/~gens http://southport.jpl.nasa.gov http://www-star.stanford.edu/sar_group/. The interferometric fringes form a map of one component of the displacement field with dense spatial sampling (>100 pixels/km^2).

To explain the observed coseismic deformation, a simple model of a dislocation in an elastic half space provides a good approximation. Indeed, it has become the conventional model used in all the case studies cited earlier.

The FORTRAN program documented in this paper, called RNGCHN for 'RaNGe CHaNge', uses this model to calculate a single component of the displacement vector at an arbitrary number of points. As such, it provides a convenient means for modeling crustal deformation. Although we have designed the program to handle satellite radar interferometric measurements of coseismic displacements, the RNGCHN program has applications for other signals measured by other geodetic techniques, as the examples below will show.

2. Assumptions

The RNGCHN program uses the dislocation formulation given in closed analytic form by Okada (1985). Accordingly, the displacement field $u_i(x_1, x_2, x_3)$ due to a dislocation $\Delta u_j(\xi_1, \xi_2, \xi_3)$ across a surface Σ in an isotropic medium is

$$u_i = \frac{1}{F}\int\int_{\Sigma} \Delta u_j \left[\lambda \delta_{jk} \frac{\partial u_i^n}{\partial \xi_n} + \mu \left(\frac{\partial u_i{}^j}{\partial \xi_k} + \frac{\partial u_i^k}{\partial \xi_j} \right) \nu_k \right] \mathrm{d}\Sigma \qquad (1)$$

where δ_{jk} is the Kronecker delta, λ and μ are Lamé's coefficients, ν_k is the direction cosine of the normal to the surface element $\mathrm{d}\Sigma$, and the summation convention applies. The term u_i^j is the ith component of the displacement at (x_1, x_2, x_3) due to the jth direction point force of magnitude F at (ξ_1, ξ_2, ξ_3). The interested reader should consult Okada (1985) for the complete set of equations, including a discussion of previous derivations.

We follow Okada's notation, as listed in Table 1. We assume that the Earth's surface is flat, corresponding to the bounding plane of an elastic half space. The Lamé coefficients λ and μ specify the elastic medium. Note that if $\lambda = \mu$, then these parameters drop out of

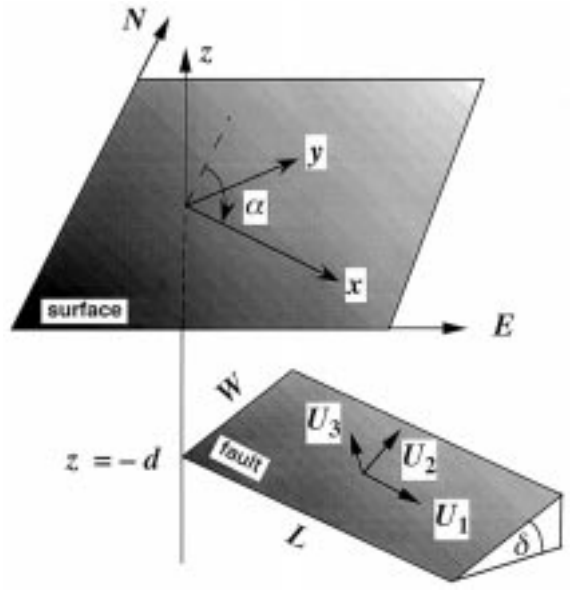

Fig. 1. Fault geometry and symbols. Slip vector $\mathbf{U}=[U_1, U_2, U_3]$ represents movement of hanging wall with respect to foot wall signed such that positive U_1 is left-lateral strike slip, positive U_2 is thrusting dip slip, and U_3 is tensile slip.

the expressions for surface displacement. Such a medium, called a Poisson solid, has a Poisson's ratio of 1/4, a reasonable approximation to the values of 0.23–0.28 estimated from P- and S-wave velocities in the upper crust (Perrier and Ruegg, 1973; Dziewonski and Anderson, 1981). In the examples shown here, we set $\lambda=\mu=1$.

2.1. Fault parameters

Although the dimensions are arbitrary, we choose a natural set of units. The dislocation may be either a point source or a rectangular fault patch of finite dimension L by W km. In either case, the slip on the fault plane is a vector with three components, U_1, U_2, U_3 in mm (Fig. 1). The origin of the fault patch lies at its lower left-hand corner when viewed from the hanging wall. The coordinates of the origin are E, N, and d, taken positive East, North, and down. To transform the (x, y) coordinate system given by Okada to the (E, N) system used by RNGCHN, we rotate by the strike (azimuth) α of the fault, in degrees clockwise from North. To avoid ambiguity, an observer facing along strike should see the fault dip at δ degrees to his right. This set of 10 parameters comprises one line of the input 'faults' file described below. One such set defines a single dislocation to describe a single fault-element (also called a 'subfault' or 'patch'). Given multiple sets, RNGCHN will calculate the total deformation from the vector sum of the surface displacements over all patches.

The Okada parameters differ slightly from the parameters favored by seismologists. In particular, the origin of Okada's fault patch does not coincide with the centroid at the geometric center of the fault rectangle. Given the coordinates (E_C, N_C, d_C) of the centroid, we find Okada's origin (E, N, d) using:

$$\begin{bmatrix} E \\ N \\ d \end{bmatrix} = \begin{bmatrix} E_C \\ N_C \\ d_C \end{bmatrix} - \frac{1}{2}\begin{bmatrix} \sin\alpha & -\cos\alpha & 0 \\ \cos\alpha & \sin\alpha & 0 \\ 0 & 0 & -1 \end{bmatrix}\begin{bmatrix} L \\ W\cos d \\ W\sin d \end{bmatrix} \quad (2)$$

We provide a simple script called SEISMO_TO_OKADA to perform this transformation in MATLAB (MathWorks, 1992) http://www.mathworks.com.

Inversely, given the coordinates (E, N, d) of Okada's origin, we find the centroid (E_C, N_C, d_C) using:

$$\begin{bmatrix} E_C \\ N_C \\ d_C \end{bmatrix} = \begin{bmatrix} E \\ N \\ d \end{bmatrix} + \frac{1}{2}\begin{bmatrix} \sin\alpha & -\cos\alpha & 0 \\ \cos\alpha & \sin\alpha & 0 \\ 0 & 0 & -1 \end{bmatrix}\begin{bmatrix} L \\ W\cos d \\ W\sin d \end{bmatrix} \quad (3)$$

The script OKADA_TO_SEISMO performs this transformation in MATLAB.

For a double-couple source, the tensile component vanishes ($U_3=0$) and the slip vector lies in the fault plane. Seismologists define the rake angle r such that $\tan r = U_2/U_1$ (Aki and Richards, 1980). Inversely, we have $r=\mathrm{ATAN2}(U_2, U_1)$ where ATAN2 is the usual FORTRAN intrinsic function for arctangent (U_2/U_1) on the range $[-180°, +180°]$. A thrust faulting mechanism, for example, has $U_2>0$ and $r>0$. A normal faulting mechanism, on the other hand, has $U_2<0$ and $r<0$. Similarly, left-lateral slip implies $U_1>0$ and $|r|\leqslant 90°$, while right-lateral slip implies $U_1<0$ and $|r|\geqslant 90°$.

The so-called 'geometric moment' or 'potency' simply equals ULW. To obtain the seismic moment, multiply by the shear modulus μ so that $M_0=\mu ULW$. Typical values for μ in the Earth's crust range from 30–36 GPa. The simplest assumption takes this value to be constant throughout the half space, although some authors propose increases with depth (Dolan et al., 1995). To convert moment into the various magnitude scales, use the conventional formulae (Hanks and Kanamori, 1979; Abe, 1995).

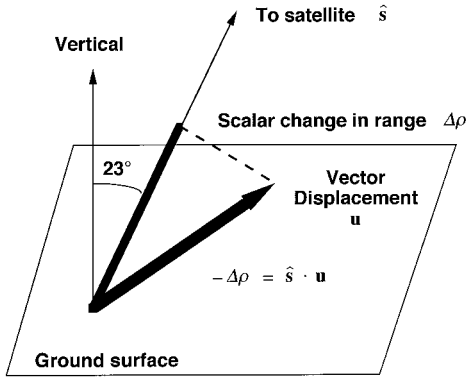

Fig. 2. Relation between vector ground displacement **u** and scalar change in range $\Delta\rho$. Unit vector $\hat{\mathbf{s}}$ points from pixel on ground toward satellite.

To choose appropriate values for the various parameters, we consult various data bases of focal mechanisms, for example, the Harvard Central Moment Tensor (CMT) catalog for events larger than magnitude about 5.5 (Dziewonski et al., 1994) http://www.seismology.harvard.edu. For smaller events, regional networks such as the Southern California Earthquake Center (Douglass and Wald, 1992) http://www.scec.org or the Northern California Earthquake Data Center (Romanowicz et al., 1994) http://quake.geo.berkeley.edu are quite useful. Empirical relations exist for establishing the size (L, W, and U) of the earthquake from the seismological magnitude or moment (Scholz, 1990; Dolan et al., 1995).

2.2. Geometric parameters

The line-of-sight between the point on the ground and the radar satellite in the sky defines two angles, the radar incidence (from vertical) and the azimuth of the satellite ground track (from North). For the ERS satellites in California, for example, these quantities are approximately 23 and 13°, respectively http://earth1.esrin.esa.it/ERS. These quantities determine the unit vector (normalized to unit length) $\hat{\mathbf{s}}$ as shown in Fig. 2. The three components of this 'look' vector are required in the 'V' (for vector) line in the input 'map' file described later.

After calculating the $\hat{\mathbf{s}}$ at the surface, RNGCHN calculates the associated change in range $\Delta\rho$ or the distance measured along the line-of-sight between the satellite and ground point with coordinates $[E, N]$. We have

$$-\Delta\rho = \mathbf{u} \cdot \hat{\mathbf{s}} \tag{4}$$

where $\hat{\mathbf{s}}$ points from ground to satellite, as shown in Fig. 2. Note that the sign convention is such that an upward movement will produce a positive value of $\mathbf{u} \cdot \hat{\mathbf{s}}$, a decrease in range, and a negative value of $\Delta\rho$.

To calculate crustal displacements measured by techniques other than satellite interferometry, we need only specify the appropriate unit vector $\hat{\mathbf{s}}$. For example, spirit leveling data provide only the vertical component of the displacement vector **u**, so we set $\hat{\mathbf{s}} = [0, 0, 1]$.

3. Examples

3.1. Simple case

To check the installation of the RNGCHN program, we provide a simple example from the original paper (Okada, 1985). Given in the first line of Table 2, the fault parameters are numbered 'Case 2' in Okada (1985). To find the East, North, and up components of the displacements, we set $\hat{\mathbf{s}}$ to [1, 0, 0], [0, 1, 0], and [0, 0, 1], respectively. Thus, we obtain the following values for $-\Delta\rho$: −136.4, −290.0, and −351.7 mm, respectively, with $U_1 = U_2 = U_3 = 10{,}000$ mm. To find these values, we sum the strike, dip, and tensile contributions given in Okada's Table 2.

Table 2
Parameter values used in examples[a]

East E (km)	North N (km)	Strike α (° CW N)	f? 0/1	Depth d (km)	Dip δ (°)	Lambda λ	Mu μ	U_1 (mm)	U_2 (mm)	U_3 (mm)	L (km)	W (km)	Name	Figure
−2.0	−3.0	90.0	1	4.0	70.	1	1	10,000.0	10,000.0	10,000.0	3.0	2.0	Test	–
0.0	0.0	106.0	1	3.4	28.0	1	1	−22.0	514.0	0.0	2.9	3.1	Thrust	3(A)
0.0	0.0	106.0	1	*6.0*	28.0	1	1	−22.0	514.0	0.0	2.9	3.1	Thrust	3(B)
0.0	0.0	*126.0*	1	3.4	28.0	1	1	−22.0	514.0	0.0	2.9	3.1	Thrust	3(C)
0.0	0.0	106.0	1	3.4	28.0	1	1	−22.0	514.0	0.0	2.9	*6.2*	Thrust	3(D)
15.6	20.2	173.0	1	12.0	54.3	1	1	−54.6	0.0	0.0	16.2	6.8	Eureka V.	4(B)

[a] The fault origin is located at (E, N, d). The fault strikes α degrees and dips at δ degrees. The dimensions of a fault patch are L by W km. The slip on the fault plane is a vector with three components, U_1, U_2, U_3 mm as shown in Fig. 1. The toggle f is 0 for a point source and 1 for a finite source.

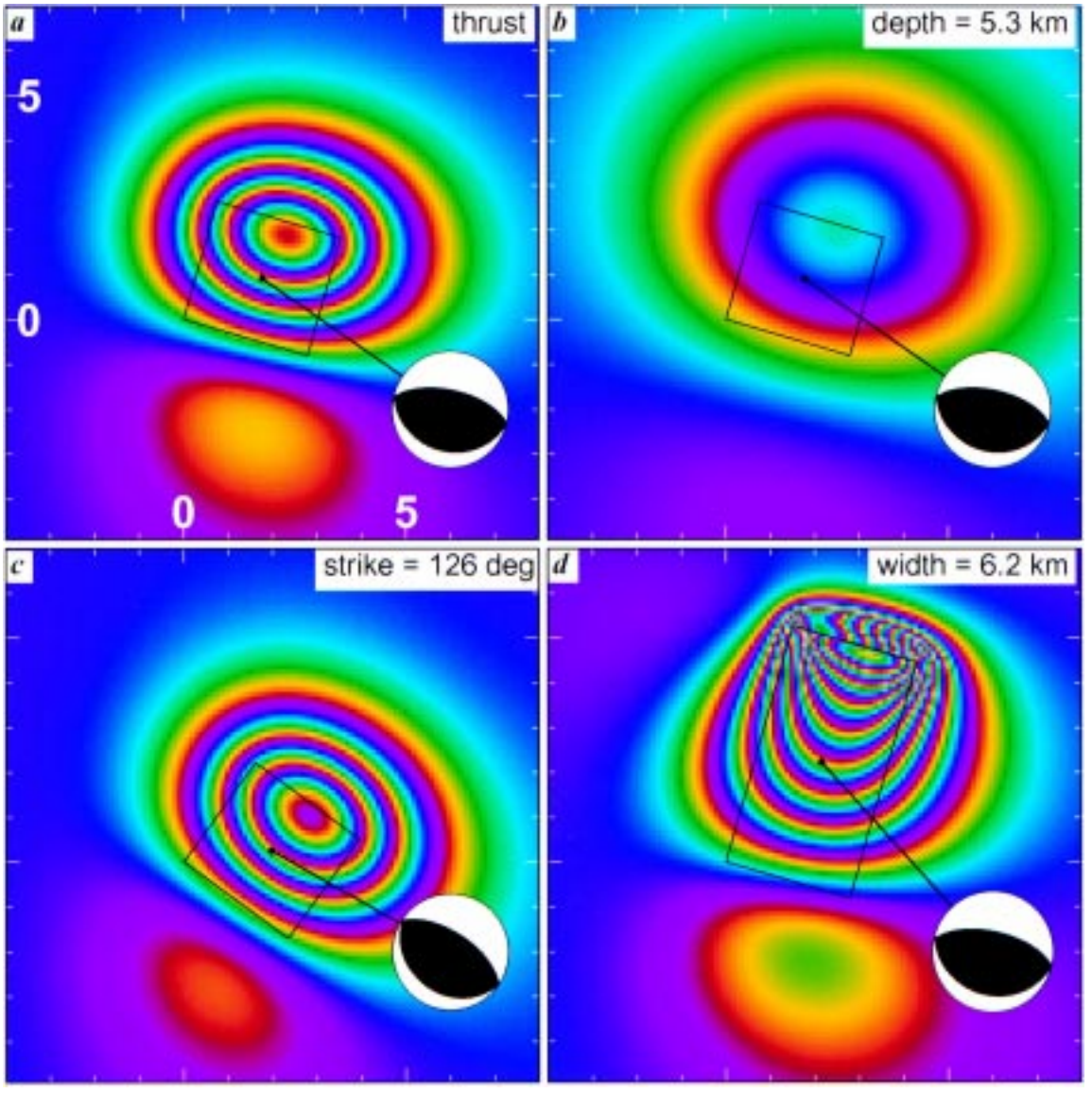

Fig. 3. Simple examples using values from lines 2–5 of Table 1. (A) Thrust fault at $d=3.4$ km depth (centroid at 2.7 km depth), $\alpha=106^\circ$ strike and $W=3.1$ km width (Feigl et al., 1995). (B) Same fault as (A), but at $d=6.0$ km depth (centroid at 5.3 km depth). (C) Same fault as (A), but at $\alpha=126^\circ$ strike. (D) Same fault as (A), but with width $W=6.2$ km. One fringe corresponds to 28 mm of range change in all four panels. Focal mechanisms show lower hemispheres with dot at centroid location. Black rectangles indicate surface projections of fault planes. Fault origin (E, N) at (0, 0) km in all four cases. Tick marks every 1 km.

3.2. Variations on a thrust

To illustrate the fringe patterns formed by various focal mechanisms, Fig. 3(A) simulates the field of range change values $\Delta\rho$ for a small $M=5.2$ earthquake in California as observed in an ERS-1 radar interferogram (Feigl et al., 1995). Subsequent panels show the effect of small variations in fault depth, strike, and width (Figs. 3(A), (C), (D), respectively).

3.3. Eureka Valley

The main shock of the Eureka Valley, California earthquake occured on 17 May 1993 with moment magnitude $M_W=6.1$. This normal-faulting event produced about a decimeter of coseismic subsidence, sufficient to measure by radar interferometry using the ERS-1 satellite (Massonnet and Feigl, 1995; Peltzer and Rosen, 1995). Fig. 4 shows the observed and mod-

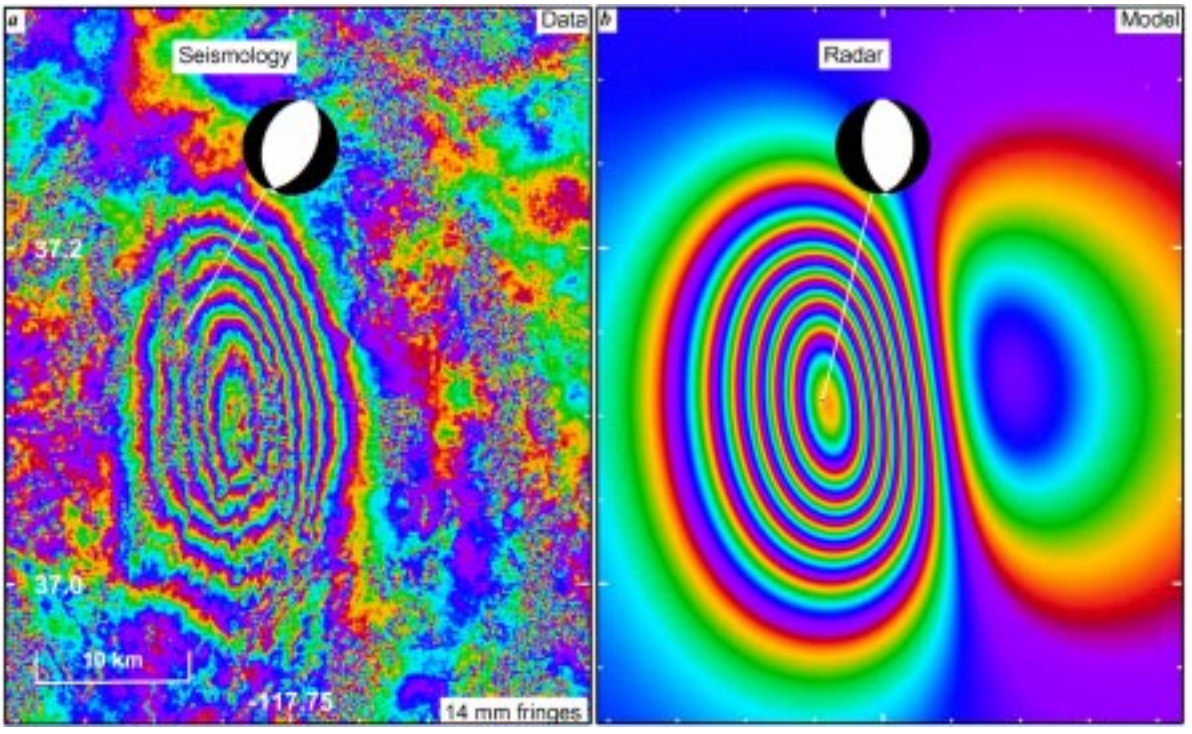

Fig. 4. Observed (left) and modeled (right) interferograms for M = 6.1 Eureka Valley, California earthquake of 17 May 1993 (Massonnet and Feigl, 1995). Seismological focal mechanism (left) was estimated by waveform modeling (Dreger, personal communication). The focal mechanism determined by radar (right) is the final estimate of a non-linear inversion scheme (Dupré, 1995; Feigl et al., 1995), for which we give model parameters in line 6 of Table 2. Estimated moment is thus 1.7×10^{18} N m (assuming a shear modulus μ of 32 GPa) for moment magnitude of 6.1. One fringe corresponds to 14 mm of range change in both panels due to stacking (Massonnet and Feigl, 1995).

eled interferograms (Massonnet and Feigl, 1995). Here, the RNGCHN program calculated the modeled interferogram and the partial derivatives were used to estimate the best-fitting fault parameters by non-linear inversion (Feigl et al., 1995; Dupré, 1995). The agreement between the observed and modeled fringe patterns is quite good, with a rms residual scatter of 7 mm.

3.4. Interseismic deformation

RNGCHN can also mimic interseismic deformation for the special case of a vertical strike-slip fault like the San Andreas. Here, the model assumes movement only below a locking depth D by extending the dislocation to infinite depth. This formulation provides the same surface displacements as a model with an elastic plate (lithosphere) of thickness D over a viscoelastic half space (asthenosphere) (Savage, 1990). To handle the coseismic case with RNGCHN, we input the annual displacement for U_1, set the dip $\delta = 90^\circ$, the depth $d = B$, and the width $W = B - D$ where B is a large numerical value representing the infinite depth of the half space. In our implementation, $B = 10{,}000$ km seems to work. Fig. 5 presents an example for interseismic crustal motion parallel to the San Andreas fault as measured by GPS (Feigl et al., 1993). To obtain the velocity parallel to the fault at 138° azimuth, we set the unit 'look' vector to follow strike horizontally $\hat{\mathbf{s}} = [\sin(138^\circ), \cos(138^\circ), 0]$ A more rigorous, but numerically expensive approach uses an edge location in a layered medium (Savage and Lisowski, 1998; Savage, 1998).

For a dipping (non-vertical) fault, one may use the same scheme (Donnellan et al., 1993), but the results may not be equivalent to the viscoelastic model (Thatcher and Rundle, 1984).

3.5. Postseismic and volcanic deformation

The elastic dislocation formulation also forms the basis of a simple model for postseismic deformation as observed in the months following the Landers earthquake (Massonnet et al., 1994; Shen et al., 1994). To handle this case, we simply set the slip vector $\mathbf{U}$ to the value expected during the time interval spanned by the

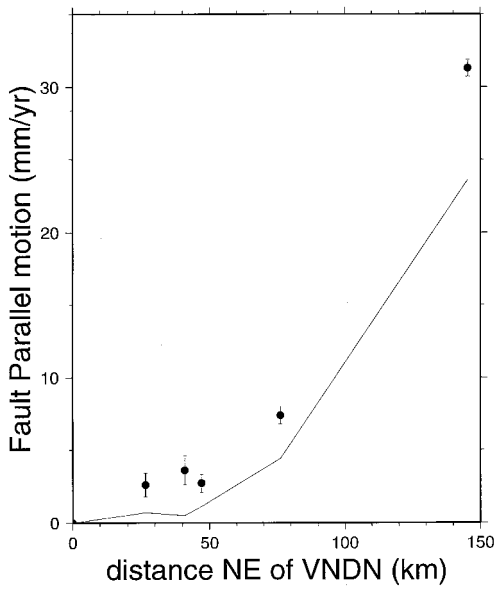

Fig. 5. Observed (points) and modeled (curve) values for rate of displacement of geodetic benchmarks parallel to San Andreas fault along profile oriented approximately normal to fault at N138°E azimuth. Observed values are space geodetic measurements of vector velocities between 1984 and 1992 (Feigl et al., 1993). Bars represent plus or minus one (scaled) standard deviation. Model curve assumes fault geometry and parameters corrected from Table 5 of Feigl et al. (1993) and give in file named fig5.faults.

observation, according to a decaying function of time (Shen et al., 1994). Alternatively, the tensile case of $U_3 < 0$ can represent the postseismic collapse of the fault zone as suggested for the Loma Prieta (Savage et al., 1994) and Landers (Massonnet et al., 1996) earthquakes.

The tensile case of $U_3 > 0$ can also represent extension of a dike in a volcanic area. One example of this case models the dikes intruded into the oceanic rift exposed in Djibouti (Stein et al., 1991).

4. Using the program

4.1. Source code

We wrote the program in standard FORTRAN 77 with a few functions in the C language to handle the binary integer output. Although the code runs on Sun, HP, and DEC workstations under UNIX, the C functions may be machine-dependent. Instructions for compiling are in the file 0README.TXT.

The program is in the public domain. To obtain a copy via Internet, use anonymous ftp to connect to spike.cst.cnes.fr IP 132.149.10.3 or ftp://spike.cst.cnes.fr/pub/GRGS/rngchn.tar.Z. The file named rngchn.tar.Z resides in the directory/pub/GRGS. To extract all the files from the archive, use the UNIX commands 'uncompress rngchn.tar.Z' followed by 'tar-xvf rngchn.tar'. Alternatively, users may request the program by sending a formatted floppy disk to the first author. The code is available on the IAMG server.

In addition to the RNGCHN program, the archive file contains all the files necessary to generate the examples shown here. We also include routines for calling RNGCHN from within MATLAB as a 'MEX-file' (MathWorks, 1992) http://www.mathworks.com.

4.2. Mapping options

The RNGCHN program requires the coordinates of points on the ground to calculate the change in range at each location. The coordinates may be listed explicitly, or implicitly as a grid. If listed, the coordinates are assumed to be cartographic easting and northing in kilometers. To specify a grid implicitly in cartographic coordinates, using the 'M' line in the input 'map' file described below. Alternatively, the implicit grid coordinates may be geographic latitude and longitude expressed in degrees with the 'G' line in the 'map' file. In this case, RNGCHN projects the geographic coordinates into cartographic coordinates with a Universal Transverse Mercator (UTM) projection on the WGS84 ellipsoid (Snyder, 1982).

4.3. Output options

The simplest use of RNGCHN is to calculate the range change at a number of ground points. For this, use the 'ascii' option to write a simple ASCII text file with a table of values. Similarly, the 'residual' option will read a list of observed values, calculate the theoretical value, and compute the difference. The program then writes all three values, with their map coordinates, in the output file. To calculate the three components of the vector displacement **u** instead of the scalar range change $-\Delta\rho$, use the 'vector' option.

To save disk space, RNGCHN can also output two styles of binary file containing a rectangular array of scalar range change values. In this case, the horizontal coordinates of each pixel are implied by order rather than an explicit list. The first pixel is at the Southwest corner; the second, one step to the East; the last one, at the Northeast corner. In other words, RNGCHN outputs the array by rows ('lines') from left (West) to right (East).

With the 'binary' option, RNGCHN writes the range change value in cycles coded such that 1 cycle = 256 digital units. Specify the number of millimeters per cycle on the 'V' line in the input 'map' file.

In this format, one pixel is a single, unsigned 1-byte integer. This representation is called 'wrapped' because it is modulo-one cycle.

With the 'mmbin2' option, RNGCHN writes the range change value in absolute millimeters coded as a signed 2-byte integer. Binary files created with this option are 'unwrapped' and thus suitable for interpolation.

To visualize the output as images, we recommend a standard graphics package such as the public-domain Generic Mapping Tools (Wessel and Smith, 1991; 1998) http://www.soest.hawaii.edu.

For inverse problems, RNGCHN can write the partial derivatives of $-\Delta\rho$ with respect to each of the 10 fault parameters in an ASCII text file with the 'partial' or 'analytic' options. The 'partial' option calculates the derivative numerically by finite differences with a step size of one unit in each parameter. It is accurate to about 10% in most instances. The 'analytic' option calculates the partial derivatives using complete analytic expressions (Dupré, 1995). Although somewhat slower than the numerical expressions, the analytic values can provide better convergence in non-linear inversion schemes (Dupré, 1995). The partial derivatives were used, for example, to estimate the focal mechanisms for the two California earthquakes shown in Figs. 3(A) and 4(B) (Feigl et al., 1995; Massonnet and Feigl, 1995).

4.4. Input map file

This file contains either a list of ground point coordinates or the specifications to create a regular rectangular grid. The coordinates [*E, N*] should be listed in the order: easting in km, northing in km, and (optionally) an observed value of $-\Delta\rho$ in mm. The observed value is required only for the 'residual' output option. The format is free, but lines with coordinates must begin with a blank in column 1. Otherwise, lines beginning with a non-blank character in column 1 trigger other options, in particular:

'V' (for vector) line. To specify the unit vector $\hat{\mathbf{s}}$, begin a line with 'V' followed by the East, North, and up components in that order. The vector should be normalized to have unit magnitude. The fourth parameter on the line is the interval between fringes in millimeters. For radar interferometry, the value should be half the radar wavelength, e.g., the fringe interval is 28.3 mm for the ERS-1 satellite. This line is required.

'G' (for 'grid') line. To specify a grid in geographic coordinates, being a line with 'G' followed by lon_0, lat_0, *dlon, dlat, nlon, nlat*, in that order. Here, the grid origin (Southwest corner) is located at longitude lon_0 degrees (East positive) and latitude lat_0 degrees (North positive). Each pixel will be *dlon* by *dlat* degrees in size. The output array contains *nlon* pixels in each row and *nlat* pixels in each column. This option requires a 'Z' line to define the cartographic parameters for the UTM projection.

'M' (for 'map') line. To specify a grid in cartographic coordinates, being a line with 'M' followed by E_0, N_0, *dE, dN, nE, nN*, in that order. Here, the grid origin (Southwest corner) is located at E_0 km easting and N_0 km northing. Each pixel will be *dE* by *dN* km in size. The output array will contain *nE* pixels in each row and *nN* pixels in each column.

'Z' (for 'zone') line. To set the cartographic parameters for the UTM projection, begin a line with 'Z' followed by *izone,* ux_0, uy_0. Here, izone is the conventional zone number (Snyder, 1982). The origin of the UTM projection is at easting ux_0 km and northing uy_0 km. This line is required if the 'G' line is used.

4.5. Input fault file

This file contains the fault parameters in the order: *X, Y,* α, *f, d,* δ, λ, μ, U_1, U_2, U_3, *L, W, name*. We have defined these parameters and their units above, with examples in Table 1. Here, the toggle *f* is 0 for a point source and 1 for a finite source. The format is free, but lines describing faults must begin with a blank in column 1. Otherwise, lines with a non-blank character in column 1 are treated as comments and ignored.

4.6. Execution

To run the program, type on the UNIX command line:

```
rngchn mapfile faultsfile outputfile option
```

where the three file names and the option are defined above. To perform the simple case given in the first example below, run:

```
rngchn teste.xyr test.faults teste.out residual
```

using the files `teste.xyr test.faults` included with the source code. The results output in `teste.out` should match those in the `teste.doc` file we provide.

To run the program from within MATLAB, issue the command

```
dr = rangechange (x,y,strike,depth,dip,u1,u2,u3,1,w,e,n,s);
```

where the first 10 variables on the right-hand-side are column vectors as defined above. The vectors `e` and `n` specify the coordinates [*E, N*] of the ground point in km. Finally, the three-component vector `s` specifies the unit 'look' vector $\hat{\mathbf{s}}$. The values returned in the column vector `dr` are $-\Delta\rho$ in mm. Calling the program with an optional second output array on the left-hand-side

will also return the matrix of partial derivatives in the array `ap`:

```
[dr, ap] =

   rangechange (x,y,strike,depth,dip,u1,u2,u3,1,w,e,n,s);
```

For additional documentation, type `range_change` with no arguments.

Acknowledgements

We are indebted to Didier Massonnet and his group at the CNES in Toulouse for developing the radar interferometric technique which created the need for this program. Wayne Thatcher, Alexis Rigo and Julia Talaya suggested improvements to the manuscript and the program. We thank Andrea Donnellan for some of the dislocation codes. E.D. appreciates her CNES internship. Figs. 3–5 were made with the public domain GMT software (Wessel and Smith, 1991; 1998). Funding from the French Programme National en Télédetection Spatiale and the European Space Agency contributed to the development. Research supported by the U.S. Geological Survey (USGS), Department of the Interior, under USGS award number 1434-95-G-2603. The views and conclusions contained in this document are those of the authors and should not be interpreted as necessarily representing the official policies, either expressed or implied, of the U.S. Government.

References

Abe, K., 1995. Moments and magnitudes of earthquakes. In: Ahrens, J. (Ed.), Global Earth Physics: A Handbook of Physical Constants, vol. 1. American Geophysical Union, Washington, DC, pp. 206–213.

Aki, K., Richards, P.G., 1980. Quantitative Seismology. W.H. Freeman, San Francisco, 932 pp.

Clark, T.A., Ma, C., Sauber, J.M., Ryan, J.W., Gordon, D., Shaffer, D.B., Chaprette, D.S., Vandenberg, N.R., 1990. Geodetic measurement of deformation in the Loma Prieta, California earthquake with very long baseline interferometry. Geophysical Research Letters 17 (8), 1215–1218.

Dolan, J.F., Sieh, K., Rockwell, T.K., Yeats, R.S., Shaw, J., Suppe, J., Huftile, G.J., Gath, E.M., 1995. Prospects for larger or more frequent earthquakes in the Los Angeles metropolitan region. Science 267 (5195), 199–205.

Donnellan, A., Hager, B.H., King, R.W., 1993. Discrepancy between geological and geodetic deformation rates in the Ventura Basin. Nature 366, 333–336.

Douglass, K., Wald, L., 1992. Southern California Earthquake Data Center. EOS Transactions of American Geophysical Union 73 (51), 548.

Dupré, E. 1995 Application de l'interféremoétrie radar aux phénomènes géophysiques, D.E.A. Université P. Sabatier, Toulouse, France, 39 pp.

Dziewonski, A.M., Anderson, D.L., 1981. Preliminary reference Earth model. Physics of the Earth Planetary Interior 25, 297–356.

Dziewonski, A.M., Ekström, G., Salganik, M.P., 1994. Centroid-moment tensor solutions for October–December, 1993. Physics of the Earth Planetary Interior 85 (3), 215–225.

Feigl, K.L., Agnew, D.C., Bock, Y., Dong, D., Donnellan, A., King, R.W., Hager, B.H., Herring, T.A., Jackson, D.D., Jordan, T.H., Larsen, S., Larson, K.M., Murray, M.H., Shen, Z., 1993. Space geodetic measurement of crustal deformation in central and southern California, 1984–1992. Journal of Geophysical Research 98, 21,677–21,712.

Feigl, K.L., Sergent, A., Jacq, D., 1995. Estimation of an earthquake focal mechanism from a satellite radar interferogram: application to the 4 December 1992 Landers aftershock. Geophysical Research Letters 22 (9), 1037–1048.

Hanks, T.C., Kanamori, H., 1979. A moment magnitude scale. Journal of Geophysical Research 84 (B5), 2348–2350.

Hudnut, K.W., Bock, Y., Cline, M., Fang, P., Feng, Y., Freymuller, J., Ge, X., Gross, W.K., Jackson, D., Kim, M., King, N.E., Langbein, J., Larsen, S.C., Lisowski, M., Shen, Z.-K., Svarc, J., Zhang, J., 1994. Coseismic displacements of the 1992 Landers earthquake sequence. Bull. Seism. Soc. Amer. 84 (3), 625–645.

Lin, J., Stein, R.S., 1989. Coseismic folding, earthquake recurrence, and the 1987 source mechanism at Whittier Narrows, Los Angeles basin, California. Journal of Geophysical Research 94 (B7), 9614–9632.

Massonnet, D., Feigl, K.L., 1995. Satellite radar interferometric map of the coseismic deformation field of the M = 6.1 Eureka Valley, California earthquake of 17 May 1993. Geophysical Research Letters 22 (12), 1541–1544.

Massonnet, D., Feigl, K.L., 1998. Radar interferometry and its application to changes in the Earth's surface. Reviews Geophysics 36 (4), 441–500.

Massonnet, D., Feigl, K.L., Rossi, M., Adragna, F., 1994. Radar interferometric mapping of deformation in the year after the Landers earthquake. Nature 369, 227–230.

Massonnet, D., Rossi, M., Carmona, C., Adragna, F., Peltzer, G., Feigl, K., Rabaute, T., 1993. The displacement field of the Landers earthquake mapped by radar interferometry. Nature 364, 138–142.

Massonnet, D., Thatcher, W., Vadon, H., 1996. Detection of postseismic fault zone collapse following the Landers earthquake. Nature 382, 612–616.

MathWorks, 1992. MATLAB Reference Guide. The Mathworks Inc, Natik, Massachussetts.

Okada, Y., 1985. Surface deformation to shear and tensile faults in a half-space. Bulletin of the Seismological Society of America 75 (4), 1135–1154.

Peltzer, G., Rosen, P., 1995. Surface displacement of the 17 May 1993 Eureka Valley, California earthquake observed by SAR interferometry. Science 268, 1333–1336.

Perrier, G., Ruegg, J.C., 1973. Structure profonde du Massif Central français. Annals of Geophysics 29 (4), 435–502.

Romanowicz, B., Neuhauser, D., Bogaert, B., Oppenheimer,

D., 1994. Accessing Northern California Earthquake Data via Internet. EOS Transactions of the American Geophysical Union 75 (23), 257–260.

Savage, J.C., 1983. Strain accumulation in Western United States. Annual Reviews Earth Planetary Sciences 11, 11–43.

Savage, J.C., 1990. Equivalent strike–slip earthquake cycles in half-space and lithosphere–asthenosphere Earth models. Journal of Geophysical Research 95, 4873–4879.

Savage, J.C., 1998. Displacement field for an edge dislocation in a layered half-space. Journal of Geophysical Research 103 (B2), 2439–2446.

Savage, J.C., Lisowski, M., 1998. Viscoelastic coupling model of the San Andreas Fault along the big bend, southern California. Journal of Geophysical Research 103 (B4), 7281–7292.

Savage, J.C., Lisowski, M., Svarc, J.L., 1994. Postseismic deformation following the 1989 (M = 7.1) Loma Prieta, California earthquake. Journal of Geophysical Research 99, 13,757–13,765.

Scholz, C.H., 1990. In: Earthquakes and Fault Mechanics, . Cambridge University Press, Cambridge, p. 439.

Shen, Z., Jackson, D., Feng, Y., Kim, M., Cline, M., 1994. Postseismic deformation following the 1992 Landers earthquake. Bulletin of the Seismological Society of America 84, 780–791.

Snyder, J.P., 1982. In: Map projections used by the U.S. Geological Survey, 2nd ed., . U.S. Government Printing Offices, Washington, DC, p. 313.

Stein, R.S., Briole, P., Ruegg, J-C., Tapponnier, P., Gasse, F., 1991. Contemporary, Holocene, and Quaternary deformation of the Asal rift, Djibouti: implications for slow-spreading ridges. Journal of Geophysical Research 96, 21,789–21,806.

Thatcher, W., Rundle, J.B., 1984. A viscoelastic coupling model for the cyclic deformation due to periodically repeated earthquakes at subduction zones. Journal of Geophysical Research 89, 7631–7640.

Wessel, P., Smith, W.H.F., 1991. Free software helps map and display data. EOS Transactions of the American Geophysical Union 72 (41), 441.

Zebker, H.A., Rosen, P.A., Goldstein, R.M., Gabriel, A., Werner, C.L., 1994. On the derivation of coseismic displacement fields using differential radar interferometry: the Landers earthquake. Journal of Geophysical Research 99, 19,617–19,634.